Experimental Study of Carbon Sequestration Reactions Controlled by the Percolation of CO_2-Rich Brine through Peridotites

M. ANDREANI,*,† L. LUQUOT,† P. GOUZE,† M. GODARD,† E. HOISÉ,‡ AND B. GIBERT†

Géosciences, UMR 5243, Université Montpellier 2, CNRS, 34095 Montpellier, France, and Laboratoire de Géologie, Ecole Normale Supérieure, 75231 Paris, France

Received July 3, 2008. Revised manuscript received November 10, 2008. Accepted November 11, 2008.

Carbonation of ultramafic rocks in geological reservoirs is, in theory, the most efficient way to trap CO_2 irreversibly; however, possible feedback effects between carbonation reactions and changes in the reservoir permeability must be considered to realistically assess the efficiency and sustainability of this process. We investigated changes in the hydrodynamic properties of sintered dunite samples by means of percolation experiments, under conditions analogous to that of in situ carbonation. Our results show that carbonation efficiency is controlled by the local renewal of the reactants and the heterogeneity of the pore structure. Preferential flow zones are characterized by the formation of magnetite and of a silica-rich layer at the olivine surfaces, which eventually inhibits olivine dissolution. Conversely, sustainable olivine dissolution together with coprecipitation of magnesite, siderite, and minor Mg-TOT-phyllosilicates, occur in reduced-flow zones. Thus carbonate precipitation only decreases porosity in zones where diffusion-controlled transport is dominant. Consequently, while high flow rates will decrease the carbonation efficiency of the reservoir and low flow rates may reduce the permeability irreversibly close to the injection point, moderate injection rates will ensure a partial carbonation of the rock and maintain the reservoir permeability.

Introduction

In situ CO_2 sequestration is highly recommended as an effective means of significantly decreasing CO_2 concentration in the atmosphere. This method consists of injecting (supercritical) CO_2 directly into underground geological formations where it can be retained by hydrodynamic trapping, through dissolution in brines or by carbonation, i.e., transformation to carbonates. The latter represents a method of sequestering CO_2 in a lasting manner because carbonates are stable over geological time periods (*1, 2*). In situ carbonation requires the concomitant dissolution of Mg, Ca, and Fe-rich silicates (*3, 4*). Sedimentary rocks, with the exception of zeolite-rich layers, contain little Mg, Ca, and Fe-rich silicates in contrast to basaltic and ultramafic rocks (peridotites, serpentinites). Ultramafic rocks comprise mainly olivine and pyroxene; they contain 40−50 weight % MgO ± CaO ± FeO and have the highest potential for carbonation (*4*). Ultramafic bodies are abundant worldwide, on land as greenstone belts and ophiolites, and on the ocean floor at slow-spreading ridges (e.g., Atlantic Ocean). They represent a huge CO_2 potential sink capacity through exothermic alteration reactions, similar to those occurring in natural media (e.g., Figure 1), that could be triggered by industrial injection at depth (*5*−*7*). For example, the carbonation of olivine (forsterite) can be written:

$$\underset{\text{Forsterite}}{Mg_2SiO_4} + 2CO_2 \rightarrow 2\,\underset{\text{Magnesite}}{MgCO_3} + \underset{\text{Silica}}{SiO_2} \qquad (+95\ \text{kJ/mol}\ CO_2)$$

$$(44\ \text{cm}^3/\text{mol}) \quad (2\times 30\ \text{cm}^3/\text{mol}) + (23\ \text{cm}^3/\text{mol})$$

Yet, until now, research has focused mainly on industrial ex situ applications (*8, 9*), measuring the kinetics of the dissolution/carbonation reaction as a function of P_{CO_2} (*10*−*12*) and evaluating optimal conditions for ex situ olivine carbonation (*9, 13*). Experimental studies mainly used batch reactor methods, i.e., olivine grains immersed in controlled water compositions at a given pressure, temperature, and CO_2 partial pressure (P_{CO_2}). Results indicate that up to 50% carbonation can be achieved in less than an hour under optimum conditions, i.e., in saline bicarbonate-rich solutions with P_{CO_2} ranging from 11.5 to 19 MPa, and temperature (T) between 155 and 185 °C (*9, 14*). Yet, the required thermal activation and inherent production of silica-rich wastes strongly limit the industrial value of ex situ carbonation.

Alternatively, in situ carbonation in large ultramafic aquifers (e.g., Oman ophiolite (*15*), Italian Alps (*16*)) or ultramafic-hosted seafloor hydrothermal systems (*17*) is potentially a valuable strategy. Predicting the efficiency and sustainability of the process is, however, a critical issue for

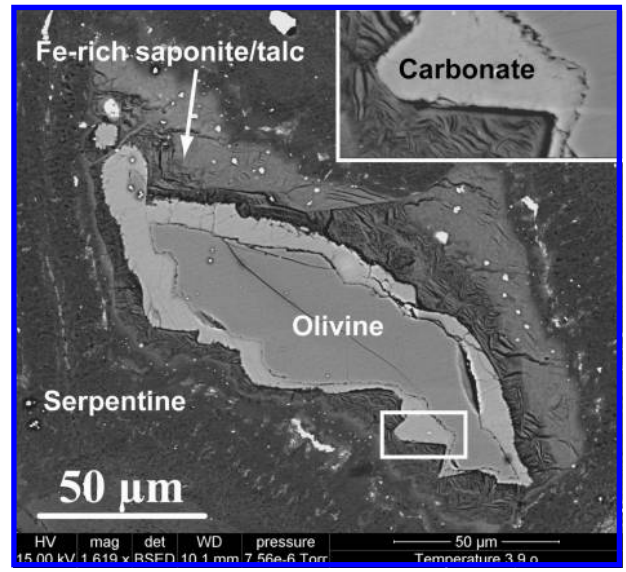

FIGURE 1. Natural carbonation of olivine in a sample from Atlantis Massif, 30°N Mid-Atlantic ridge (IODP Expedition 304). Mg-rich calcite replaces olivine after a partial serpentinization stage. Ca-CO_2-enriched fluid percolates via the more permeable olivine−serpentine interface. Olivine carbonation is accompanied by the formation of mixed saponite/talc localized in a reaction corona that fixes part of the excess Si, Mg, and Fe resulting from carbonation.

* Corresponding author now at: Laboratoire des Sciences de la Terre, UMR5570 CNRS-ENS-UCB Lyon1, 69622 Villeurbanne, France; e-mail: muriel.andreani@univ-lyon1.fr; phone: +33 (0)4 72 44 62 40.
† Géosciences, UMR 5243, Université Montpellier 2, CNRS.
‡ Laboratoire de Géologie, Ecole Normale Supérieure.

10.1021/es8018429 CCC: $40.75
Published on Web 01/07/2009

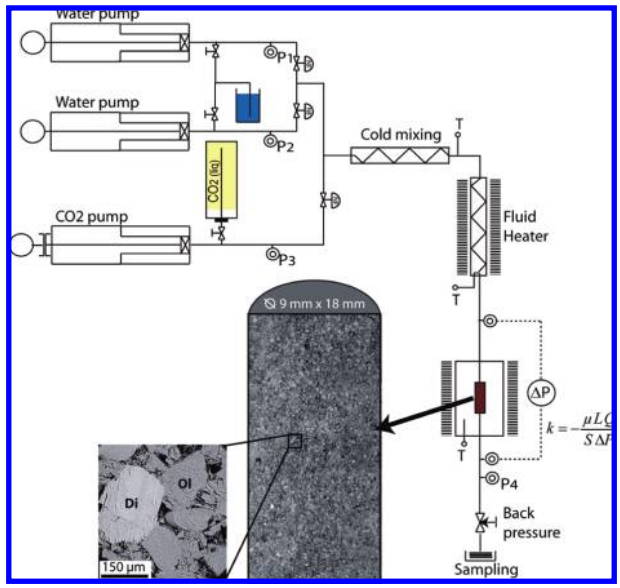

FIGURE 2. Schematic diagram of the experimental percolation bench. A SEM image of a longitudinal section of a sintered ground dunite sample is given with a zoom on grain texture (Ol = olivine; Di = diopside).

the success of in situ carbonation in ultramafic reservoirs. It relies not only on the thermodynamic conditions of chemical reactions but also on their feedback effects on the reactive surface area that controls mass transfers locally, and on the reservoir porosity and permeability. This is particularly relevant for olivine carbonation since the volume increase can theoretically reach 88% (see reaction 1). Yet, the fundamental parameters characterizing the dynamics of in situ reactions of CO_2-enriched waters in ultramafic rocks are still poorly known, and we can only speculate on the added value of the method for storing large volumes of CO_2.

We investigate here the relations between rock heterogeneity, fluid flow, and chemical reactions by performing flow-through percolation experiments on sintered dunite samples under conditions previously identified as optimum for carbonation (*9*). The progress of reactions and feedback effects on porosity and permeability are assessed by repeated analyses of the effluent fluids and continuous recording of the pressure drop in the sample. Mass transfers and reaction mechanisms at the water−mineral interfaces are characterized down to the nanometer-scale by EDS-TEM (energy-dispersive spectrometry under transmission electron microscope). These results are then used to investigate the coupled effect of structural heterogeneities and injection rate on carbonation reaction efficiency.

Experimental Methods

Two identical experiments were conducted using an experimental percolation bench (Figure 2), which allows reproducing conditions analogous to that of in situ CO_2 sequestration. Both experiments consisted in injecting CO_2-enriched water at constant flow rate through cylindrical sample cores of 9 mm diameter (D) and 18 mm length (L). They were carried out at total pressure $P = 12$ MPa, temperature $T =$ 160 °C, and CO_2 partial pressure $P_{CO_2} = 11$ MPa. Sample confining pressure (radial and axial) was 110% of the total injection pressure.

The CO_2-enriched water was made up using deionized water enriched with 1 M NaCl and 0.6 M $NaHCO_3$. Before mixing with CO_2, the pH value was 8.2, which corresponds to the average of natural waters hosted by ultramafic formations (*16*). After mixing with CO_2, the pH value, calculated using the geochemical code CHESS (*18*), dropped to 6.7.

The Si, Mg, Ca, and Fe concentrations of inlet and outlet waters, as well as that of deionized rinsing waters, were analyzed using electrophoresis and inductively coupled plasma-atomic emission spectrophotometry (ICP-AES). The inlet and deionized rinsing waters were depleted in Si, Mg, and Ca: they had concentrations below the detection limits. In contrast, outlet waters had concentrations more than 1 order of magnitude above the detection limit, indicating the strong contribution from the reactions occurring within the samples.

Changes in sample permeability $k(t)$ were derived from the pressure drop $\Delta P(t)$ between the inlet and the outlet points of the sample according to Darcy's law, which stipulates that, for laminar flow, permeability (in m^2) scales linearly with the ratio of the volumetric flow rate Q (in $m^3 \cdot s^{-1}$) over the pressure difference ΔP (in Pa): $k = -\mu LQ/S\Delta P$ where L is the length of the sample (in m) in the flow direction, S is the cross-sectional area of the sample (in m^2), and μ is the dynamic viscosity of the water (in Pa·s).

CO_2-enriched water was injected at constant flow rate Q = 0.6 mL/min through a sintered ground dunite from the San Carlos Mine (Arizona) (Figure 2). The composition of the dunite, expressed in weight %, was 97% olivine, 2% diopside, and 1% spinel (chromite). The mean grain size was 80 μm. The chemical composition of each mineral phase was determined by electron microprobe analyses: $Mg_{1.79}Fe_{0.2}Ni_{0.01}SiO_4$ for olivine, $Ca_{0.4}Mg_{0.5}Fe_{0.05}Al_{0.1}Si_{0.95}O_3$ for diopside, and $Mg_{0.7}Cr_{0.93}Fe_{0.37}AlO_4$ for spinel. Before injecting the CO_2-enriched water, the sample porosity (measured by standard triple weight method) and permeability were 0.17 ± 0.005 and 20.0 ± 0.006 × 10^{-15} m^2, respectively. After each experimental run, detailed characterization of the sample and reactive interfaces was performed at the micrometer- to nanometer-scale using scanning (SEM) and transmission (TEM) electron microscope techniques. SEM was performed under high vacuum mode with a FEI Quanta 200 instrument equipped with a field emission gun and a dispersive X-ray system. TEM characterization with selected-area diffraction patterns and EDS nanoanalyses were performed with a JEOL 2000fx using 200 kV accelerating voltage, equipped with a Tracor Northern 5520 EDS-TEM for analyzing major elements on ca. 30-nm-diameter spots in fixed-beam mode.

Results and Discussion

The two experiments led to similar changes in permeability (Figure 3A) and outlet water chemistry. For clarity, the chemical results are illustrated only for the longest experiment (experiment #2, Figure 3B). After a short transitional period, corresponding to setting up a dispersion-induced chemical gradient in the inlet water, the permeability reached a stationary regime ($\partial k/\partial t = 0.0034$ $m^2 \cdot s^{-1}$). At the same time, Si, Mg, and Ca were steadily released from the system, indicating a continuous dissolution of both olivine and diopside. All these major elements showed an almost linear decrease in concentration with time. The outlet water composition was highly enriched in Si compared to that expected from the stoichiometric dissolution of the olivine−diopside assemblage, indicating either incongruent dissolution or precipitation of Mg−Ca-rich phase(s) in the sample. A similar excess of Si in water was observed during olivine dissolution in batch reactor experiments reported by ref *19* for pH > 9 in CO_2-free waters at 25 °C, and by ref *12* for pH > 5−6 in CO_2-enriched water at 90−150 °C. These authors (*op. cit.*) observed the formation of an Mg-rich layer on olivine grain surfaces, thus providing evidence of incongruent dissolution. In contrast, we did not observe any Mg-rich

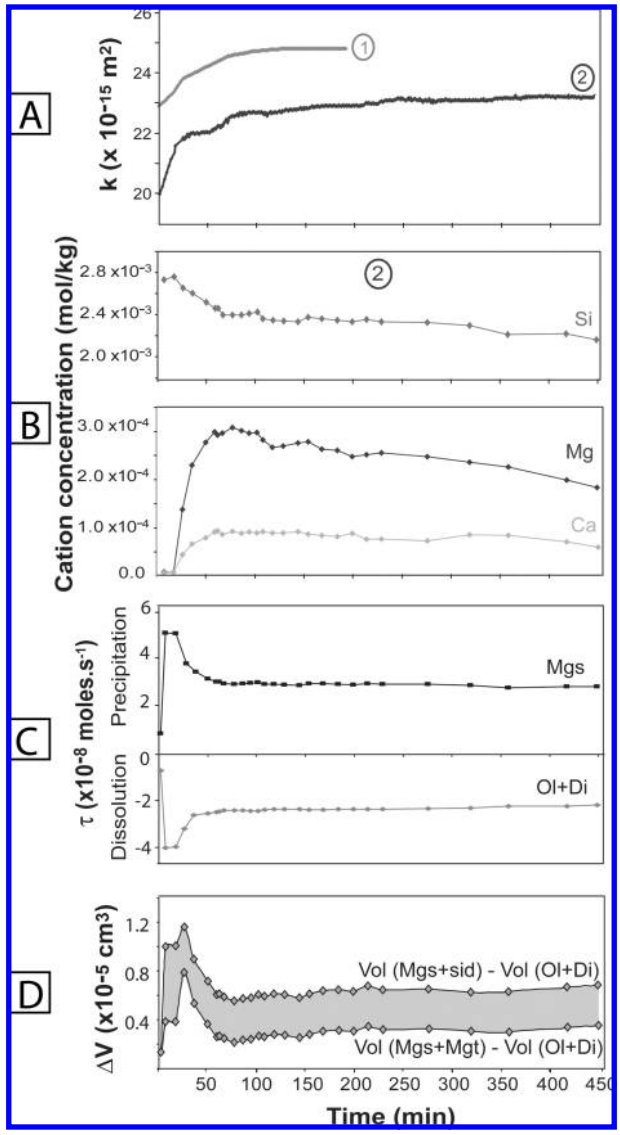

FIGURE 3. Experimental results. (A) Permeability *k* is given for the two reproducible experiments (1) and (2); the other data refer to the longer duration experiment (2) with 450 min run time. (B) The elemental concentration curves show the variation of Si, Mg, and Ca in the outlet fluid as a function of time. (C) The effective rate, τ, of the dissolution or precipitation reaction is calculated from mass balance. (D) ΔV is the total rock volume variation (volume of mineral precipitated minus volume of minerals dissolved) over the experiment; it is always positive. The shaded area indicates the possible ΔV range depending on the eventual distribution of Fe in the two types of Fe-rich products (Mgt = magnetite or sid = siderite). Ol = olivine; Di = diopside; Mgs = magnesite.

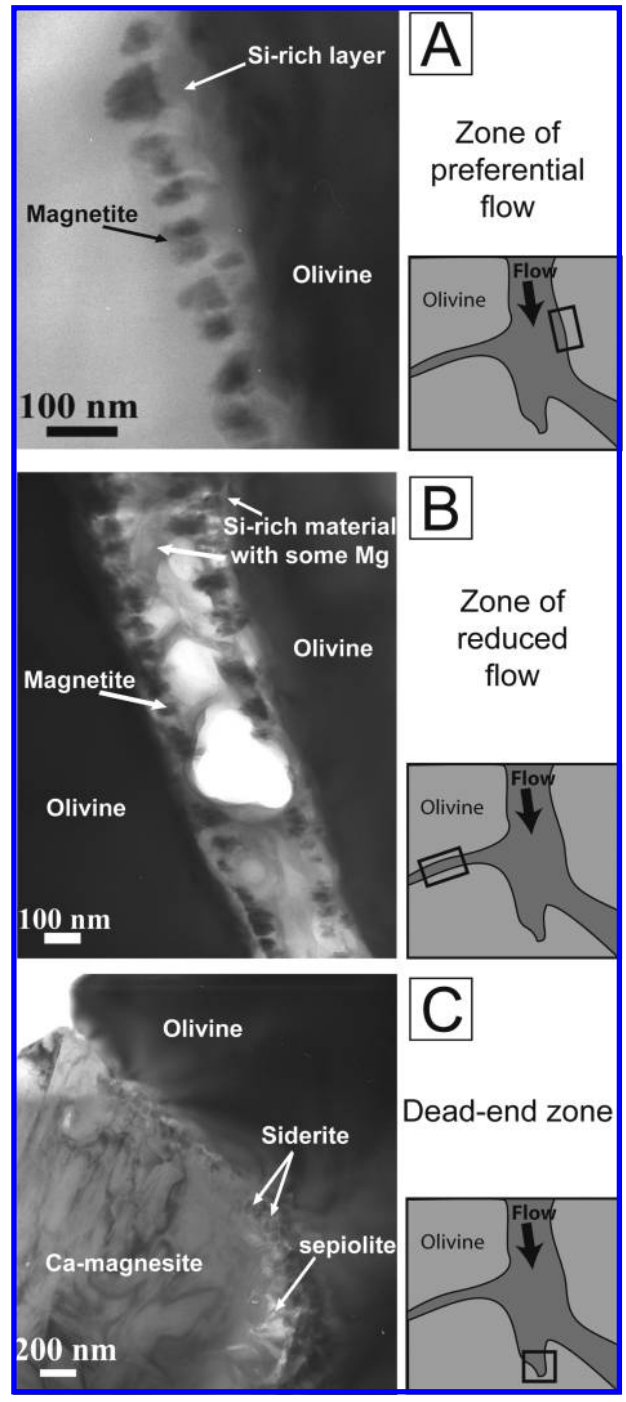

FIGURE 4. TEM images of the main reaction textures (A–C) observed in the samples after the experiment. For each reaction texture, a sketch diagram shows the main type of hydrodynamic zone in which the texture is observed and the corresponding reactants and products identified. This illustrates the variability of transport-reaction processes controlled by the structural heterogeneity of the sample.

coatings in our reacted flow-through cores; instead, we identified two types of alteration features.

The first type of alteration feature was the alignment of neoformed nanograins (up to 50 nm diameter) of magnetite (Fe_3O_4) ± minor siderite ($FeCO_3$), parallel to dissolving olivine surfaces (Figure 4A and B). The Fe-rich nanograins were always separated from the olivine surface by a Si-rich amorphous material, indicating a dissolution mechanism that preferentially released Mg into the water. Measurements of magnetic properties carried out on sample #2 showed a modification of magnetic susceptibility and magnetization, with initial values of 1.551×10^{-5} Si and 6.721×10^{-3} A/m, respectively, increasing to 1.044×10^{-4} Si and 8.886×10^{-2} A/m after the experiment, indicating the neoformation of magnetite. The oxidation of $Fe(II)^{olivine}$ to $Fe(III)^{magnetite}$ has important implications for the production of secondary gas during carbonation process, since it is usually accompanied by a reduction of H_2O to molecular H_2 ± hydrocarbons in CO_2-rich natural systems (e.g., *20, 21*).

The second alteration feature was the local growth of large Ca-enriched magnesite grains (mean structural formula $Mg_{0.9}Ca_{0.1}CO_3$, with Ca ranging from 0.09 to 0.12) on the surface of dissolving olivine grains (Figure 4C). Magnesite and olivine were separated by a nanometer-scale porous

zone partly filled with nanograins of siderite and a poorly crystallized TOT-type phyllosilicate. This phyllosilicate has a highly hydrated structure, evidenced by its rapid destabilization under the electron beam, and a stoichiometry that is close to that of talc. It is probably sepiolite, $Mg_4Si_6O_{15}(OH)_2 \cdot 6(H_2O)$, a phyllosilicate that is stable under our experimental conditions (T < 200 °C).

Knowing the mode and the composition of the initial and product minerals, the progress of the reaction was determined by mass balance between the outlet and inlet water compositions. Because the amount of silica retained in sepiolite is negligible, Si release was used as a proxy for primary mineral dissolution. Assuming the magnesite composition to be constant, the mass and reaction rate of the dissolved and precipitated minerals were calculated using the Si, Fe, Ca, and Mg breakthrough curves (Figure 3B). The effective reaction rates (τ in mol·s^{-1}), i.e., the dissolution rate of the primary reactants (here, olivine + diopside) and the precipitation rate of the main reaction product, magnesite, are illustrated in Figure 3C. The respective production of siderite and magnetite could not be estimated because both phases affect only the Fe budget. The total mass of dissolved phases (olivine + diopside) integrated over the whole experiment was 75.2 mg (48.3 mg olivine + 26.9 mg diopside) and corresponded to a rock volume V_d of 22.5 mm^3. The total mass of reaction products was 67 mg of magnesite (24.4 mm^3), plus 10.2 mg (magnetite only) to 15.3 mg (siderite only) of Fe-products. This corresponds to a precipitated volume V_p ranging from 26.4 to 28.3 mm^3, respectively.

Variations in the total rock volume $\Delta V(t) = V_p - V_d$ and porosity changes $\phi(t)$ are related by:

$$\phi(t) = \phi(t=0) - \int_0^{tf} \Delta V(t)\,dt/V_{tot} \quad (1)$$

As illustrated in Figure 3D, $\Delta V(t)$ is >0 indicating that porosity decreased during the whole experiment.

The beginning of the experiment was marked by the strongest decrease in porosity, corresponding to the maximum rates of dissolution and precipitation. The inlet water composition and flow rate were constant; therefore variations of olivine and diopside dissolution rates were controlled only by the area of accessible reactive surfaces. At t < 200 min, the maximum dissolution (Figure 3C) corresponded to the preferential dissolution of the small mineral fragments (∅ < 5 μm) produced during sintering. The development of large reactive surfaces due to grain cracking along the natural cleavage planes of diopside during sintering may explain the unexpectedly high reactivity of this mineral (more than 1/3 of the initial diopside was dissolved during the experiment). It may have favored also the localization of the main flow paths along diopside grains. The dissolution maximum led to a peak in water supersaturation that can explain the corresponding maximum in precipitation rate (Figure 3C), indicating a critical control of dissolution rate on precipitation rate.

Once the smallest fragments were removed, at t > 200 min, porosity change reached a quasi-stationary regime corresponding to the homogeneous dissolution of the grains. We observed a small decrease of the dissolution rate of olivine and diopside that was attributed to the reduction of the reactive surface areas resulting from the grain volume reduction and/or the decrease of the accessible reactive surface areas due to precipitation and coating.

Finally, we noted a significant increase of permeability even though porosity decreased. In the next section, the origin of this nonstandard behavior is enlightened from a detailed analysis of the chemical processes and mass transfers at microscopic scale.

Microscopic Chemical Processes and Heterogeneity. The well aligned magnetite +/− siderite grains probably represent the initial dissolution surface of olivine (Figure 4). At the end of the experiment, olivine displayed an irregular surface associated with an amorphous Si-rich layer 30−70 nm thick displaying a sharp contact with the underlying unaltered olivine surface. Béarat et al. (*22*) recently reported the formation of an ∼40 nm thick Si-rich layer, characterized by an abrupt contact with olivine, during batch-reactor dissolution experiments under similar *P-T-* P_{CO_2} conditions. The origin and properties of such Si-rich layers at the surface of dissolving silicate minerals are still a matter of debate. Si-rich layers are usually interpreted as the result of electrophilic reactions at the olivine surface, leading first to the formation of >Si−OH surface groups associated with a preferential release of Mg^{2+}, which is then exchanged with $2H^+$ in solution. This interdiffusion model implies incongruent dissolution during which the Si-rich leached layer becomes structurally stabilized by condensation or polymerization of the silanol groups via >Si−O−Si< bonding onto a gel layer at the mineral surface (*23*). Recent investigations (*24*) of feldspar dissolution propose an alternative interfacial dissolution−reprecipitation model in which the stoichiometric dissolution of the mineral is followed immediately by the precipitation of a hydrated silica gel at the water−mineral interface. In both cases, once the gel is formed, it must be permeable to allow transport of ions and water by diffusion toward and away from the reactive interface, so as to maintain the reaction. BET measurements of the effective surface area (*25*) and numerical modeling (*22*) indicate that the gel layer can be regarded as a zone with continuous permeable regions through which the effective diffusion rate will depend on the gel porosity and tortuosity. The development of a diffusion-limited Si-rich layer, which progressively advances through the core and possibly radially around grains, will affect the transport of the reactants and reduce the fluid accessibility to the reactive surfaces, thus decreasing the effective dissolution rate of olivine (Figure 3C). In addition, condensation or polymerization due to >Si−O−Si< bonding is expected to induce a progressive densification of the structure of the Si-rich layer with time, which will inhibit transport through this layer. In natural systems, this surface passivation will contribute to a downstream shift of the main reaction front to zones rich in fresh olivine surfaces. While this process ensures spatial extension of the reaction, complete carbonation of the rock will necessarily be limited.

Texture and chemical analyses indicated a strong chemical heterogeneity of the reactive interfaces within the same sample, in zones sometimes separated by only a few micrometers. Carbonate precipitation is favored in domains of reduced water flow, such as dead-end zones, where chemical gradients are small and thus facilitate local cation supersaturation (Figure 4C), higher pH, and more reducing conditions. Reduced flow zones are characterized by the growth of magnesite, +/− siderite and sepiolite, at the expense of olivine (Figure 4C) by dissolution−precipitation processes similar to those observed in natural samples (Figure 1). Carbonate grains nucleate on olivine surfaces and their growth is fed by both local (i.e., adjacent olivine dissolution) and distant sources since the magnesite always contains some Ca (produced elsewhere by diopside dissolution). In contrast, strong local chemical gradients develop at the mineral/water interface in zones of preferential flow, thus favoring total leaching of Mg (Figure 4A), except for negligible Mg retained within the Si-rich layer in narrower interstices (Figure 4B). In addition, precipitation of magnetite in high water flow zones (Figure 4A), as opposed to siderite precipitation in more confined zones (Figure 4C), implies that Fe oxidation is favored by water renewal and that redox gradients exist at the sample scale.

Traces of Al were detected by EDS-TEM at the olivine−magnesite interface, thus providing evidence that this

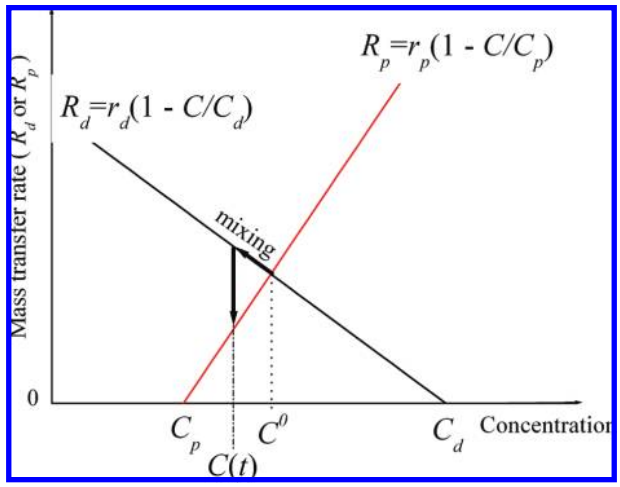

FIGURE 5. Mass transfers associated with olivine dissolution and magnesite precipitation (here assumed to be linear; $n = n' \neq 1$) versus Mg concentration in the vicinity of the reaction zone. Hydrodynamic mixing of the dissolution effluent with the bulk water (with low or zero Mg concentration) will lead to dilution and thus decrease the local efficiency of the olivine-to-magnesite transformation.

interface remained accessible to water and reactants during the experiment. This implies that precipitation of the siderite−sepiolite assemblage does not inhibit olivine dissolution, although mass transfers were probably mostly diffusive in these zones. On the contrary, the formation of the siderite−sepiolite assemblage allows maintaining the reactivity of the olivine interface and thus the sustainability of carbonation reactions. In contrast, high flow zones were marked first by high dissolution rates then the development of Si-rich passivation layers on olivine reactive surfaces. The modal and grain size distribution heterogeneities of the sample (close to the values expected in natural systems) led to the establishment of the preferential flow paths, which ensured efficient spreading of CO_2-rich fluids throughout the whole sample. At the same time, flow heterogeneities developed thus allowing localizing the main reaction products outside of these preferential flow paths. It followed that both the permeability and the rock volume increased at the same time (Figure 3A and D). These self-organizing flow-reaction processes will ensure the sustainability of carbonation reactions in the structurally heterogeneous natural media.

Water Flow Control on Carbonation Efficiency. Let us evaluate the carbonation efficiency $\eta(p(r))$ of a microscale reaction site $p(r)$, a pore−olivine interface located at the macroscale distance r from the injection point. As long as carbon remains in excess in the fluid, $\eta(p(r))$ can be defined as the efficiency of the olivine-to-magnesite transformation:

$$\eta(p(r)) = R_p(p(r))/R_d(p(r)) \quad (2)$$

where $R_d(p(r))$ (in $mol \cdot s^{-1} \cdot m^{-3}$) is the dissolution rate of olivine (assumed here first order):

$$R_d(p(r)) = \kappa_d \times (1 - C(p(r))/C_d) \quad (3)$$

with $C(p(r))$ the Mg concentration at site $p(r)$, κ_d ($\kappa_d > 0$) the effective dissolution kinetic coefficient and C_d the Mg concentration at-equilibrium with olivine. Similarly, $R_p(p(r))$, the precipitation rate of magnesite, is:

$$R_p(p(r)) = \kappa_p \times (1 - C(p(r))/C_p) \quad (4)$$

with κ_p ($\kappa_p < 0$) the effective precipitation kinetic coefficient and C_p the Mg concentration at-equilibrium with magnesite. Carbonation happens when $C_p < C_d$ (Figure 5).

If no hydrodynamic mixing would occur with the bulk water (i.e., the flow-in water far from reaction site $p(r)$), the concentration would be stationary, $C(p(r)) = C_0$, where C_0 is given by solving $R_d = R_p$, and the carbonation efficiency would be 1. However, carbonation requires the transport of the carbon from the bulk water to the reaction site $p(r)$ and consequently hydrodynamic mixing controls the reaction rate. It follows that carbonation efficiency is lower than 1. The Mg concentration at site $p(r)$ can be approximated by the mixing relationship:

$$C(p(r)) \equiv (\alpha(p(r)) \times C_b(r)) + (1 - \alpha(p(r))) \times C_0 \quad (5)$$

where $C_b(r)$ is the bulk water Mg concentration at the distance r from the injection and $\alpha(p(r))$ is the local mixing coefficient. Carbonation efficiency $\eta(p(r))$ is a function of $\alpha(p(r))$:

$$\eta(p(r)) = \kappa_p \times \left(1 - \frac{(\alpha(p(r)) \times C_b(r)) + (1 - \alpha(p(r))) \times C_0}{C_p}\right) / \kappa_d \times \left(1 - \frac{C_0}{C_d}\right) = 1 - \frac{\alpha(p(r)) \times (C_0 - C_b(r))}{C_{ref}} \quad (6)$$

where $C_{ref} = \kappa_d \times C_p \times (C_0 - C_d)/(\kappa_p \times C_d)$ is a constant characterizing the local geochemical system under consideration independently of the pore geometry. For smooth laminar flow, $\alpha(p(r))$ is proportional to the local Peclet number

$$Pe(p(r)) = \frac{u(r) \times \lambda(p(r))}{d} \quad (7)$$

with d the diffusion coefficient, $\lambda(p(r))$ the distance between dissolution and precipitation locations, and $u(r)$the average velocity in the bulk water. It follows that the local carbonation efficiency is:

$$\eta(p(r)) = 1 - \left[\left(\frac{G(p(r))}{C_{ref}}\right) \times Pe(p(r)) \times (C_0 - C_b(r))\right] \quad (8)$$

where $G(p(r))$ is a parameter characterizing the local geometrical configuration of the mixing zone (similar to the Taylor coefficient). Equation 8 shows that the carbonation efficiency at site $p(r)$ depends on the bulk water Mg concentration $C_b(r)$. Along flow paths, the bulk water will be progressively enriched in Mg (i.e., $C_0 - C_b(r)$ decreases). Consequently, the carbonation efficiency is expected to increase with the distance r from the injection point as long as carbon is in excess in the bulk water. Conversely, equations 7 and 8 show that carbonation will be the most efficient (i.e., $\eta \rightarrow 1$) when magnesite precipitates close to the olivine dissolution zone $\lambda \rightarrow 0$ and/or in zones where diffusion-controlled transport dominates advective transport ($\lambda < d$), for instance, in zones poorly connected to the main flow (Figure 4C).

At the reservoir-scale, the macroscopic CO_2 carbonation efficiency simplifies to r-dependent variables:

$$\eta(r) = 1 - [F \times u(r) \times (C_0 - C_b(r))] \quad (9)$$

with

$$F = \frac{1}{d \times C_{ref}} \times \langle G(p(r)) \times \lambda(p(r)) \rangle_{p(r)} \quad (10)$$

where $\langle . \rangle_{p(r)}$ denotes the averaged value of the geometrical properties of the reaction sites located at a distance r. For a macroscopically homogeneous reservoir, Fcan be assumed constant.

For a radial cylindrical geometry (CO_2 injection from a portion of length Hin the well), the flow velocity $u(r)$ decreases with distance according to:

$$u(r) = \frac{1}{2 \times \pi \times \phi \times H} \times \frac{Q_{inj}}{r} \quad (11)$$

where Q_{inj} and ϕ are the injection rate ($m^3 \cdot s^{-1}$) and the porosity. For a given porosity and injector size H, the injection rate will determine the distance at which the optimal carbonation condition occurs (i.e., a moderate value of the Peclet number). While our experimental results show that a partial carbonation of the rock does not alter the permeability, it can be anticipated from the increase of the molar volume (see equation 1) that diffusion dominant transport in the bulk water should decrease porosity dramatically. Consequently, a very low injection rate may reduce the permeability irreversibly close to the injection point, whereas a high flow rate will increase the surface passivation and reduce the carbonation potential of the rock. A more quantitative evaluation of the optimal injection rate, taking into account the changes in porosity and reactive surface area, requires further long-lasting experiments at different flow rates.

Acknowledgments

We thank two anonymous reviewers for their constructive comments. TEM work was made possible by the National Instrument Facility for Earth Science Project. This work was funded by the French National Agency for Research (ANR).

Literature Cited

(1) Seifritz, W. CO_2 disposal by means of silicates. *Nature* **1990**, *345*, 486.
(2) Bachu, S.; Gunter, W. D.; Perkins, E. H. Aquifer disposal of CO_2: Hydrodynamic and mineral trapping. *Energy Convers. Manage.* **1994**, *35*, 269–279.
(3) Lackner, K. S.; Wendt, C. H.; Butt, D. P.; Joyce, E. L.; Sharp, D. H. Carbon Dioxide Disposal in Carbonate Minerals. *Energy* **1995**, *20*, 1153–1170.
(4) Xu, T.; Apps, J. A.; Pruess, K. Numerical simulation of CO_2 disposal by the mineral trapping in deep aquifers. *Appl. Geochem.* **2004**, *19*, 917–936.
(5) Berner, R. A.; Lasaga, A. C.; Garrels, R. M. The carbonate-silicate geochemical cycle and its effect on atmospheric carbon dioxide over the past 100 millions years. *Am. J. Sci.* **1983**, *283*, 641–683.
(6) Brady, P. V.; Gislason, S. R. Seafloor weathering controls on atmospheric CO_2 and global climate. *Geochim. Cosmochim. Acta* **1997**, *61*, 965–973.
(7) Alt, J.; Teagle, D. A. H. The uptake of carbon during alteration of oceanic crust. *Geochim. Cosmochim. Act* **1999**, *63*, 1527–1535.
(8) Goff, F.; Lackner, K. S. Carbon Dioxide Sequestering Using Ultramafic Rocks. *Environ. Geosci.* **1998**, *5*, 89–101.
(9) O'Connor, W. K.; Dahlin, D. C.; Nilsen, D.N.; Rush, G. E.; Walters, R. P.; Turner, P. C. Carbon Dioxide Sequestration by Direct Mineral Carbonation: Results from Recent Studies and Current Status. Presented at *First National Conference on Carbon Sequestration*, Washington, DC, May 14−17, 2001.
(10) Schulze, R.; Hill, M. A.; Field, R. D.; Papin, P. A.; Hanrahan, R. J.; Byler, D. D. Characterization of carbonated serpentine using XPS and TEM. *Energy Convers. Manage.* **2004**, *45*, 3169–3179.
(11) Giammar, D. E.; Bruant, R. G., Jr.; Peters, C. A. Forsterite dissolution and magnesite precipitation at conditions relevant for deep saline aquifer storage and sequestration of carbon dioxide. *Chem. Geol.* **2005**, *217*, 257–276.
(12) Hanchen, M.; Prigiobbe, V.; Storti, G.; Seward, T. M.; Mazzotti, M. Dissolution kinetics of forsteritic olivine at 90−150 °C including effects of the presence of CO_2. *Geochim. Cosmochim. Acta* **2006**, *70*, 4403–4416.
(13) Guthrie, G. D.; Carey, J. W.; Bergfeld, D.; Byler, D.; Chipera, S.; Ziock, H.-J. Geochemical Aspects of the Carbonation of Magnesium. Presented at *First National Conference on Carbon Sequestration*, Washington, DC, May 14−17, 2001.
(14) O'Connor, W. K.; Dahlin, D. C.; Rush, G. E.; Gederman, S. J.; Penner, L. R. Energy and economic considerations for ex-situ aqueous mineral carbonation In *Proceedings of the 29th International Technical Conference on Coal Utilization and Fuel Systems*, 2004, p 71.
(15) Matter, J.; Kelemen, P. Enhanced Natural Carbon Sequestration in Tectonically Exposed Mantle Peridotites. *Eos Trans. AGU* **2007**, (52), 1380; Fall Meet. Suppl., Abstract U43C.
(16) Cipolli, F.; Gambarella, B.; Marini, L.; Ottonello, G.; Vetuschi Zuccolini, M. Geochemistry of high-pH waters from serpentinites of the Gruppo di Voltri (Genova, Italy) and reaction path modeling of CO_2 sequestration in serpentinites aquifers. *Appl. Geochem.* **2004**, *19*, 787–802.
(17) Carpenter, T. M.; Kaszuba, J. P. In-situ Carbonation of Magnesium Silicates: an Experimental Investigation of the Sequestration Potential of Oceanic Crust. *Eos Trans. AGU* **2007**, (52), 1381; Fall Meet. Suppl., Abstract U43C.
(18) Van der Lee, J.; De Windt, L.; Lagneau, V.; Goblet, P. Presentation and application of the reactive transport code HYTEC. *Dev. Water Sci.* **2002**, *47*, 599–606.
(19) Pokrovsky, O. S.; Schott, J. Kinetics and mechanism of forsterite dissolution at 25 °C and pH from 1 to 12. *Geochim. Cosmochim. Acta* **2000**, *64*, 3313.
(20) Holm, N. G.; Charlou, J.-L. Initial indications of abiotic formation of hydrocarbons in the Rainbow ultramafic hydrothermal system, Mid-Atlantic Ridge. *Earth Planet. Sci. Lett.* **2001**, *191*, 1–8.
(21) Sleep, N. H.; Meibom, A.; Fridriksson, Th.; Coleman, R. G.; Bird, D. K. H2-rich fluids from serpentinization: geochemical and biotic implications. *Proc. Natl. Acad. Sci. U.S.A.* **2004**, *101*, 12818–12823.
(22) Béarat, H.; McKelvy, M. J.; Chizmeshya, A. V. G.; Gormley, D.; Nunuez, R.; Carpenter, R. W.; Squires, K.; Wolf, G. H. Carbon sequestration via aqueous olivine mineral carbonation: role of passivating layer formation. *Environ. Sci. Technol.* **2006**, *40*, 4802–4808.
(23) Casey, W. H.; Westrich, H. R.; Banfield, J. F.; Ferruzzi, G.; Arnold, G. W. Leaching and reconstruction at the surfaces of dissolving chain-silicates minerals. *Nature* **1993**, *366*, 253–255.
(24) Hellmann, R.; Penisson, J.-M.; Hervig, R. L.; Thomassin, J.-H.; Abrioux, M.-F. An EFTEM/HRTEM high-resolution study of the near surface of labradorite feldspar altered at acid pH: evidence for interfacial dissolution-reprecipitation. *Phys. Chem. Minerals* **2003**, *30*, 192–197.
(25) Casey, W. H.; Westrich, H. R.; Massis, T.; Banfield, J. F.; Arnold, G. W. The surface of labradorite feldspar after acid hydrolysis. *Chem. Geol.* **1989**, *78*, 205–218.

ES8018429